Computers and Fluids 196 (2020) 104348

Contents lists available at ScienceDirect

Computers and Fluids

journal homepage: www.elsevier.com/locate/compfluid

Application of recurrence CFD (rCFD) to species transport in turbulent vortex shedding

S. Abbasi [a,b,c], S. Pirker [a,b], T. Lichtenegger [a,b,*]

[a] Department of Particulate Flow Modelling, Johannes Kepler University, Linz, Austria
[b] Linz Institute of Technology (LIT), Johannes Kepler University, Linz, Austria
[c] K1-MET Metallurgical Competence Center, Linz, Austria

ARTICLE INFO

Article history:
Received 21 March 2019
Revised 24 September 2019
Accepted 23 October 2019
Available online 24 October 2019

Keywords:
Large eddy simulations
Recurrence statistics
Multi-scale problems
Time-extrapolation
Recurrence CFD
Data-assisted simulation

ABSTRACT

The functionality of computational fluid dynamics (CFD) for turbulent flows is limited by huge computational demands which prevent any detailed long-term studies. In this publication, we apply the recently introduced, data-assisted method "recurrence CFD" (rCFD) to turbulent vortex shedding after a circular cylinder at Reynolds number $Re = 3900$. Using a database of flow fields from short, conventional simulations, we time-extrapolate their behavior to arbitrary durations and obtain promising results for passive species transport with speed-up factors of more than 120 at 1/20 of the required computer power compared to the underlying large eddy simulation (LES). Besides this massive run-time reduction, we focus on data efficiency. For cases with strong, spatial scale separation, rCFD's resilience towards grid coarsening allows us to carry out calculations at lower mesh resolution provided one retains meso-scale velocity fluctuations as a contribution to diffusivity. This reduces database size which would otherwise become a bottleneck in the methodology.

1. Introduction

The drastic increase of available computer power has extended the scope of applicability of CFD from simple two-dimensional single-phase flows to complex, transient, three-dimensional multiphase flows even under highly turbulent conditions. To solve such problems, there are several well-established techniques [1] including direct numerical simulation (DNS), large eddy simulations (LES) and Reynolds-averaged Navier-Stokes simulations (RANS). Performing DNS is highly expensive since they solve the Navier-Stokes equations directly in the entire domain and resolve the whole temporal and spatial scales of the flow down to the Kolmogorov length [2–4]. The computational cost can be reduced by solving just the large and intermediate scales and modeling the influence of the smaller ones, which is done in LES [5]. However, still the essential range of time-scales and length-scales for LES limits their use to low and moderate Reynolds numbers. RANS models require lower spatial and temporal resolution, however they bring an additional loss of information due to statistical averaging [6].

Put differently, with increasing cell size, the employed sub-grid corrections need to capture more of the ongoing physics on smaller scales by modeling the effect of the corresponding degrees of freedom without any explicit calculation. An alternative approach to eliminate inessential degrees of freedom was inspired by the experimental observation of coherent structures in turbulent flows [7–9]. These are characteristic spatial features which reappear in an irregular fashion but exhibit a distinctive temporal evolution. A huge body of research emerged trying to extract such structures and obtain their equations of motion using techniques like proper orthogonal decomposition (POD) or dynamic mode decomposition (DMD) (cf. the reviews [10,11]).

While the high computational costs per time step and their large number prevent long-term investigations of transient problems using LES or unsteady RANS despite intense research activity [12–17], reduced-order Galerkin models built from POD modes are numerically much cheaper but suffer from long-time [18–25] and other types of instabilities [26–31] that require additional handling.

In this work, we want to apply the recent approach rCFD [32] to turbulent problems to overcome the limitation of costly computations. Based on the characteristic temporal life-cycle of dominant flow structures, rCFD aims to time-extrapolate the phase-space tra-

Abbreviations: CFD, computational fluid dynamics; DMD, dynamic mode decomposition; DNS, direct numerical simulation; LES, large eddy simulation; PIV, particle image velocimetry; POD, proper orthogonal decomposition; RANS, Reynolds-averaged Navier-Stokes; RQA, recurrence quantification analysis; rCFD, recurrence CFD.

* Corresponding author at: Department of Particulate Flow Modelling, Johannes Kepler University, Linz, Austria.
E-mail addresses: sanaz.abbasi@jku.at (S. Abbasi), stefan.pirker@jku.at (S. Pirker), thomas.lichtenegger@jku.at (T. Lichtenegger).

https://doi.org/10.1016/j.compfluid.2019.104348
0045-7930/

Nomenclature

Greek letters

Δ	filter width
Δt	time step
θ	angle
ν	viscosity
ρ	density
τ	time range
$\boldsymbol{\tau}^{\mathrm{c}}$	residual scalar flux
$\boldsymbol{\tau}^{\mathrm{r}}$	residual stress tensor
$\boldsymbol{\Omega}$	vorticity

Latin symbols

C	species, constant, coefficient
D	diameter, distance norm/matrix
$\mathcal{D}$	diffusivity
E	mean interval steps
F/G	filter function
$\mathbf{F}$	force
f	frequency
k	residual kinetic energy
L	length
$\mathcal{N}$	distance norm's normalization constant
P	jump probability
p	pressure
R	recurrence norm/matrix
Re	Reynolds number
r	radius
$\mathbf{r}/\boldsymbol{x}$	position
$\boldsymbol{S}$	rate of strain tensor
Sc	Schmidt number
St	Strouhal number
$\mathcal{S}$	source term
t	time
U_∞	free stream velocity
$\mathbf{u}$	velocity
x	stream-wise direction
y	transverse direction
z	span-wise direction

Subscripts/Superscripts

b/e	begin/end
bin.	binary
c	cells
D/L	drag/lift
F/G	filter
i	interval i
rec	recurrence
rms	root mean square
sep	separation
sgs	sub-grid scale
sim	similar state
vs	vortex shedding
∞	free stream
$-$	filtered
$\langle\,\rangle$	averaged

jectory of systems exhibiting recurring patterns, e.g. vortices behind blunt bodies, according to recurrence plots introduced by Eckmann et. al. [33] and later formalized in the recurrence quantification analysis (RQA) [34,35]. Using fields from an initial, short, detailed simulation (regardless if DNS, LES or RANS), the long-time evolution is approximated assuming that similar configurations will show similar short-term behavior. Essentially, a large number of flow field sequences are chained in a smooth fashion, which amounts in an iterated method of analogues [36].

Although the fields can have the same high level of spatial resolution as the underlying simulation, time-extrapolation is extremely cheap. Not even a set of mode equations of motion needs to be solved. At the same time, no stability problems occur since only information from the reliable, initial simulation is employed. These properties make the method very interesting for long-time studies of passive or weakly coupled processes on highly dynamic backgrounds, e.g. species transport in a turbulent flow.

Here, to examine the proper functionality of rCFD in turbulent flows, we want to answer two questions: a) Is it possible to capture turbulent long-time transport behavior based on small initial data sets? b) Without the need to solve the fluid momentum equation and to take care of pressure-velocity coupling, how much can we reduce temporal and spatial resolution and still get accurate results with respect to species distribution? To this end, we test our methodology on the well-studied case of vortex shedding behind a circular cylinder with available experimental data to validate our detailed simulation results.

We first review the fluid equations of motion and describe the rCFD procedure in Section 2. Next, Section 3 illustrates main parameters and the setup of the full and the rCFD simulations. Then, we show data validation of the LES calculation, investigate the flow's recurrent behavior, present simulation results of species transport using rCFD and carry out a performance analysis in Section 4. The final Section 5 points to conclusions of the work and gives an outlook on future activities.

2. Theoretical background

Here, we briefly review the set of equations governing a single-phase, incompressible flow from the LES perspective and describe the rCFD approach. While rCFD can be applied under compressible conditions in a straight-forward fashion, we restrict ourselves to the incompressible, divergence-free case in the present work for the sake of simplicity.

2.1. Fluid equations of motion

The system of equations considered for an incompressible, single-phase fluid along with passive transport of a scalar concentration C are

$$\nabla \cdot \mathbf{u} = 0 \tag{1}$$

$$\frac{\partial \mathbf{u}}{\partial t} + (\mathbf{u}\cdot\nabla)\mathbf{u} = -\frac{1}{\rho}\nabla p + \nabla\cdot\nu\nabla\mathbf{u} \tag{2}$$

$$\frac{\partial C}{\partial t} + (\mathbf{u}\cdot\nabla)C = \nabla\cdot\mathcal{D}\nabla C + \mathcal{S} \tag{3}$$

where diffusivity

$$\mathcal{D} = \frac{\nu}{Sc} \tag{4}$$

is connected to viscosity ν via the Schmidt number Sc, and $\mathcal{S}$ is a constant source term. As mentioned in Section 1, LES is one of the methods to numerically simplify the Navier-Stokes equations through a filtering operation

$$\bar{\mathbf{u}}(\mathbf{x},t) \equiv \int d\mathbf{r}\, G(\mathbf{r},\mathbf{x})\mathbf{u}(\mathbf{x}-\mathbf{r},t). \tag{5}$$

Applying the kernel $G(\mathbf{r},\mathbf{x})$ to Eqs. (1) – (3), the set of filtered equations can be written as

$$\nabla\cdot\bar{\mathbf{u}} = 0 \tag{6}$$

$$\frac{\partial \bar{\mathbf{u}}}{\partial t} + (\bar{\mathbf{u}} \cdot \nabla)\bar{\mathbf{u}} = -\frac{1}{\rho}\nabla \bar{p} + \nabla \cdot \nu \nabla \bar{\mathbf{u}} - \nabla \cdot \boldsymbol{\tau}^{\mathrm{r}} \tag{7}$$

$$\frac{\partial \bar{C}}{\partial t} + (\bar{\mathbf{u}} \cdot \nabla)\bar{C} = \nabla \cdot \mathcal{D} \nabla \bar{C} - \nabla \cdot \boldsymbol{\tau}^{\mathrm{c}} + \bar{\mathcal{S}} \tag{8}$$

where the residual stress tensor $\boldsymbol{\tau}^{\mathrm{r}} \equiv \overline{\mathbf{u}\mathbf{u}} - \bar{\mathbf{u}}\bar{\mathbf{u}}$ and the residual scalar flux $\boldsymbol{\tau}^{\mathrm{c}} \equiv \overline{\mathbf{u}C} - \bar{\mathbf{u}}\bar{C}$ require closure [1]. Introducing the sub-grid scale viscosity ν_{sgs}, the Boussinesq approach postulates the simple relationship

$$\boldsymbol{\tau}^{\mathrm{r}} = -2\nu_{\mathrm{sgs}}\bar{\mathbf{S}} \tag{9}$$

between the residual stresses and the filtered rate-of-strain tensor

$$\bar{\mathbf{S}} \equiv \frac{1}{2}\left(\nabla \bar{\mathbf{u}} + \left(\nabla \bar{\mathbf{u}}\right)^{T}\right). \tag{10}$$

Based on dimensional arguments, one can make an ansatz

$$\nu_{\mathrm{sgs}} = C_{\mathrm{k}}\sqrt{k}\Delta \tag{11}$$

in terms of the residual kinetic energy $k \equiv \frac{1}{2}(\overline{\mathbf{u}\cdot\mathbf{u}} - \bar{\mathbf{u}}\cdot\bar{\mathbf{u}})$, the filter width Δ which is the cube root of cell volume and a model coefficient C_{k}. Among the large number of models to obtain k from available quantities, we chose a simple, algebraic approach following Smagorinsky [37], which is based on the assumption of local equilibrium between the production and dissipation of turbulent kinetic energy and leads to [1]

$$k = \frac{2C_{\mathrm{k}}}{C_{\epsilon}}\Delta^2 \bar{\mathbf{S}} : \bar{\mathbf{S}} \tag{12}$$

$$C_{\mathrm{k}} = 0.094 \tag{13}$$

$$C_{\epsilon} = 1.048. \tag{14}$$

Analogous to the residual stress tensor, we can model the residual scalar flux with the gradient diffusion hypothesis

$$\boldsymbol{\tau}^{\mathrm{c}} = \mathcal{D}_{\mathrm{sgs}} \nabla \bar{C}. \tag{15}$$

Although most generally, sub-grid diffusivity can show some degree of anisotropy and hence $\mathcal{D}_{\mathrm{sgs}}$ is a tensor [38–41], recent studies [42,43] have pointed out that LES predict transport mechanisms with a scalar sub-grid diffusivity $\mathcal{D}_{\mathrm{sgs}} = \nu_{\mathrm{sgs}}/Sc_{\mathrm{sgs}}$ accurately, whereas RANS require an anisotropic treatment.

We stress that the methodology presented in the following sections is completely independent of the specific choice of $\mathcal{D}_{\mathrm{sgs}}$ and, more generally, may be applied with any turbulence model to generate the velocity fields for the database.

2.2. Recurrence-based time extrapolation

The main objective of rCFD is time-extrapolation of a system's behavior based on information from a short-time, detailed simulation while maintaining a high degree of accuracy. Therefore, to start with rCFD, it is essential to record a sufficient amount of data comprising the required flow fields over a certain time range τ_{rec} during which the fields are stored with a specified sampling time interval Δt_{rec}. The latter needs to be chosen such that the flow does not change considerably within Δt_{rec} in order to solve the transport equation. τ_{rec} is rarely known a priori, e.g. if the flow is driven by a single dominant frequency. Otherwise, it needs to be determined from the recurrence statistics (see below).

2.2.1. Recurrence statistics

To quantify a system's degree of recurrence, a distance norm [32], e.g.

$$D(t,t') \equiv \left[\frac{1}{\mathcal{N}}\int d^3r\left(\mathbf{u}(\mathbf{r},t) - \mathbf{u}(\mathbf{r},t')\right)^2\right]^{\frac{1}{2}} \tag{16}$$

normalized by

$$\mathcal{N} \equiv \max_{t,t'}\int d^3r\left(\mathbf{u}(\mathbf{r},t) - \mathbf{u}(\mathbf{r},t')\right)^2 \tag{17}$$

compares velocity fields at two times for all $N = \tau_{\mathrm{rec}}/\Delta t_{\mathrm{rec}}$ times stored in the database giving rise to the distance matrix

$$D_{m,n} \equiv D(m\Delta t_{\mathrm{rec}}, n\Delta t_{\mathrm{rec}}). \tag{18}$$

The lower values in the distance matrix represent the similarity between two states, and vice versa. Moreover, one can obtain various characteristic numbers of the system from the distance matrix, e.g. the mean nearest-neighbor distance

$$D_{\mathrm{sim}} \equiv \frac{1}{N}\sum_{m}^{N}\min_n D_{m,n}. \tag{19}$$

The saturation or rather the appearance of plateaus of D_{sim} or of RQA parameters with database size can be used to estimate sensible values of τ_{rec}.

Alternatively, Eqs. (16) and (18) may be reformulated in terms of a recurrence norm and matrix,

$$R(t,t') \equiv 1 - D(t,t') \tag{20}$$

$$R_{m,n} \equiv 1 - D_{m,n}, \tag{21}$$

respectively. The binary version of Eq. (21), $R^{(\mathrm{bin.})}_{m,n}(\varepsilon) \equiv \Theta(\varepsilon - D_{m,n})$, has been used extensively in literature. Among various target systems, recurrence plots and statistics have also been employed to analyze turbulent flows [44–50].

In the following section, we show how one can utilize them to approximate their temporal evolution.

2.2.2. Recurrence path

Time evolution of a recurrent flow is obtained from a recurrence path on the recurrence statistics. As explained in previous work [32], one starts at a given begin time with the corresponding original flow data. After generating a time interval of random length (see below for details) with consecutive fields, the state of the interval end is identified with the most similar past one in the distance matrix. Likewise, after a certain number of steps in the database from that state on, the flow field is updated based on the minimum value of distance norm in the distance matrix for the end of the second interval and so on.

For some cases, it is advantageous to generate a recurrence path from two or more separate databases, e.g. because of various possible process states [51,52] or to enforce certain constraints, which we model as a Markov process. For example, the reflection symmetry of time-averaged vortex shedding in geometries with the same symmetry is not fully recovered from a limited number of pseudo-periods due to turbulent fluctuations. However, based on this knowledge, we can record a database $D^{(1)}$ for a small number of cycles and guarantee symmetry of the final results by extending it with its mirrored counterpart $D^{(2)}$ to give $D = D^{(1)} \cup D^{(2)}$. Compared to the case of a single database, the only difference is that the continuous time intervals cannot range from one into another. One can set a "jump probability" P to obtain a desired mean interval length $\mathrm{E}(\Delta t_i/\Delta t_{\mathrm{rec}}) = (1-P)/P$ well below the database size, e.g. 1/4 of it, but still large enough to take intervals of multiple consecutive steps. We go from one state to that Δt_{rec} later

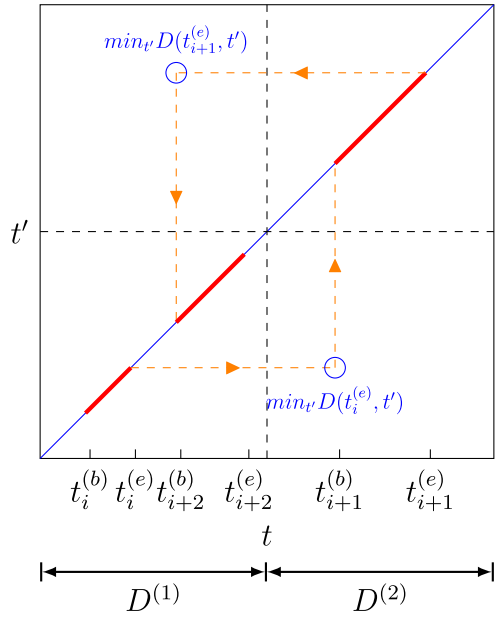

Fig. 1. Recurrence path generated for two separate databases. Sequences of intervals of consecutive time steps are connected via jumps in the recurrence statistics. The database for finding the next interval, i.e. the minimum value in the distance matrix, is selected randomly according to predefined weights.

with probability $1 - P$ unless it corresponds to the end of the current database $D^{(m)}$. Otherwise, a jump in the recurrence statistics is performed. First, based on their predefined, relative weights, either the same or a new database $D^{(n)}$ is selected and then, the most similar flow configuration is looked up in the distance matrix. Ultimately, this procedure which is depicted in Figs. 1 and 2 gives a sequence of intervals $[t_i^{(b)}, t_i^{(e)} = t_i^{(b)} + \Delta t_i]$, $[t_{i+1}^{(b)}, t_{i+1}^{(e)} = t_{i+1}^{(b)} + \Delta t_{i+1}]$, $\dots$, with mean length $\mathrm{E}(\Delta t_i/\Delta t_{\mathrm{rec}})$. According to the recurrence path generated from these intervals, the corresponding original flow data is used to go on with the process resulting in time series of the form

$$\mathbf{u}\left(\mathbf{r}, t_i^{(b)}\right), \mathbf{u}\left(\mathbf{r}, t_i^{(b)} + \Delta t_{\mathrm{rec}}\right), \cdots, \\ \mathbf{u}\left(\mathbf{r}, t_i^{(e)}\right) \approx \mathbf{u}\left(\mathbf{r}, t_{i+1}^{(b)}\right), \mathbf{u}\left(\mathbf{r}, t_{i+1}^{(b)} + \Delta t_{\mathrm{rec}}\right), \cdots. \tag{22}$$

2.2.3. Recurrence CFD

After acquiring the recurrence path, we can study any passive process like species transport by solving only a single convection-diffusion equation

$$\frac{\partial C}{\partial t} + (\mathbf{u}_{\mathrm{rec}} \cdot \nabla) C = \nabla \cdot \mathcal{D}_{\mathrm{rec}} \nabla C + \mathcal{S} \tag{23}$$

with the information recorded in the database ($\mathbf{u}_{\mathrm{rec}}$ and $\mathcal{D}_{\mathrm{rec}}$). The diffusivity $\mathcal{D}_{\mathrm{rec}}$ contains contributions from the molecular and the sub-grid scale diffusivities $\mathcal{D}$ and $\mathcal{D}_{\mathrm{sgs}}$. If the mesh used for rCFD is the same as the one built for LES, one can write

$$\mathcal{D}_{\mathrm{rec}} = \mathcal{D} + \mathcal{D}_{\mathrm{sgs}}, \tag{24}$$

and directly save and use $\mathcal{D}_{\mathrm{sgs}}$ in the database. However, since here only species transport is of importance and there is no need to solve the momentum and pressure equations, we may use a much coarser grid onto which we map the recorded flow fields before solving Eq. (23). While computationally much cheaper, the transition from the fine LES to the coarse rCFD mesh introduces a new closure problem. We need not only include sub-grid scale fluctuations already taken care of by $\mathcal{D}_{\mathrm{sgs}}$ but also retain fine-grid scale ones due to the second filtering operation.

There are at least two strategies to obtain $\mathcal{D}_{\mathrm{sgs}}$ for the coarser grid. In the paper, we chose to use an LES closure model like

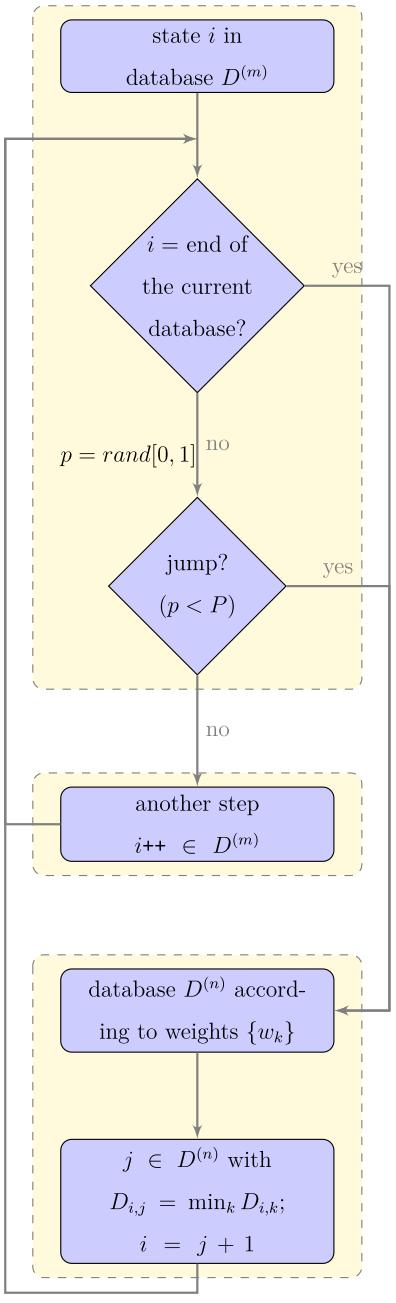

Fig. 2. Flow chart for creating a recurrence path. For each step, it has to be decided if a jump is performed or not, and if so, into which database.

Eqs. (11) and (15) on the new mesh. Following Germano [53,54], "given two filters F and G, the residual stress tensor at FG level, $\tau_{FG}(u_i, u_j) = \langle u_i u_j \rangle_{FG} - \langle u_i \rangle_{FG} \langle u_j \rangle_{FG}$, is equal to the G-averaged value of the residual stress at the F level plus the resolved turbulent stress extracted from the resolved scale F",

$$\tau_{FG}(u_i, u_j) = \langle \tau_F(u_i, u_j) \rangle_G + \tau_G(\langle u_i \rangle_F, \langle u_j \rangle_F). \tag{25}$$

If we consider our two filters as the LES one and the grid coarsening (C) for rCFD, the residual kinetic energy of the coarser mesh can be computed as

$$k_C = \left\langle k + \frac{1}{2} \bar{\mathbf{u}} \cdot \bar{\mathbf{u}} \right\rangle_C - \frac{1}{2} \langle \bar{\mathbf{u}} \rangle_C \cdot \langle \bar{\mathbf{u}} \rangle_C \tag{26}$$

in terms of the LES sub-grid kinetic energy k and the fine grid velocity $\bar{\mathbf{u}}$. We can use an LES model and calculate the sub-grid diffusivity for the coarsened mesh based on the sub- and fine-grid

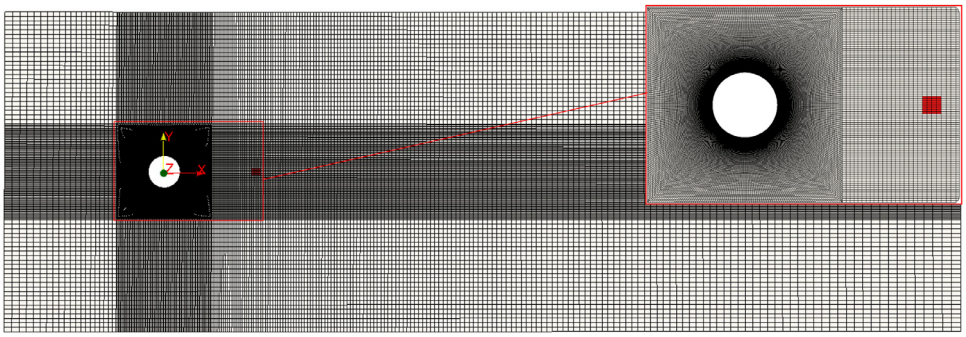

Fig. 3. Illustration of the computational grid created for LES referred to as "L1". The number of the cells is about 3.85×10^6. The fine grid region and the source location are magnified.

Table 1
Geometric dimensions of the computational domain.

Domain parameter	Length
L_x	$30D$
L_y	$10D$
L_z	πD

kinetic energy k provided by the recurrence database, e.g.

$$\mathcal{D}_{sgs} = \frac{C_k \sqrt{k_C} \Delta}{Sc_{sgs}}. \tag{27}$$

Clearly, this method eventually becomes unreliable for very coarse grids. As an alternative to our approach employing Eq. (27), one could directly save the sub- and fine-grid diffusivity of passive transport from the LES simulation with respect to the coarser grid [43]. Such a strategy would also allow to use other turbulence models than those employing eddy viscosities, e.g. deconvolution-based ones [55,56], for the generation of the database. However, we stress that the resulting sub-grid diffusivity needs to be obtained from the initial simulation and not during the rCFD run with grids being far too coarse for any deconvolution operations. It is worth mentioning that for the first approach – provided we utterly trust rCFD –, there is no requirement of solving the passive transport equation (8) during LES, whereas in the second strategy, we would be forced to include species transport in the data-generating calculations.

3. Simulation setup

Our case of study to apply the method to a turbulent flow was vortex shedding after cylinder with diameter D in a sub-critical flow regime [57,58] at $Re \equiv U_\infty D/\nu = 3900$. In this section, we describe the setups of the LES and the rCFD simulations. In several aspects, the former is aligned with other studies [59–61] with respect to the flow configuration and comparing the results.

3.1. LES

The set of equations was solved using the PISO algorithm [62,63] with the OpenFOAM toolbox. The computational grid built for this case (in the following referred to as "L1") is presented in Fig. 3, and has about 3.85×10^6 cells. The dimensions of the domain are listed in Table 1. The mesh was resolved near the cylinder to avoid using wall functions ($\Delta r/D = 0.001$), and the inlet boundary condition was considered to be laminar [59–61]. A cell set at $x/D = 2.85$ with the length of $0.3D$ was created for the purpose of adding a constant source of species. The sub-grid and laminar Schmidt numbers were set to 0.7 and 0.9, respectively. A time step of $\Delta t_{LES} = 10^{-3} D/U_\infty$ was sufficiently small to ensure a Courant number of less than 0.3. The discretization scheme of the transient term was first-order implicit Euler, those applied for pressure gradient, convection and diffusion term were second-order central difference [63].

Table 2
Computational grids and sampling times employed in rCFD. The number of nodes are reduced proportionally from R1 to R3 with reference to L1.

Spatial resolution	
$N_{c;\,L1}$	3.85×10^6
$N_{c;\,R1}$	7.68×10^5
$N_{c;\,R2}$	4.75×10^5
$N_{c;\,R3}$	2.65×10^5
Sampling frequency	
f_{rec}/f_{vs}	450
f_{rec}/f_{vs}	90
f_{rec}/f_{vs}	45

3.2. rCFD

As mentioned in Section 2.2, if one is not interested in smallest-scale details, it is possible to perform rCFD on a coarser mesh because only the passive transport equation needs to be solved. We built three different grids referred to as "R1", "R2" displayed in Fig. 4 and "R3" by proportionally decreasing the number of nodes relative to L1 with the aim of studying the method's efficiency and its limit in grid coarsening.

In addition to grid size, another factor affecting the performance was the recurrence sampling time Δt_{rec}. As explained in Section 2.2, the flow information should not change too strongly from one time step to the next. In other words, the recording frequency f_{rec} for which we tested three different values had to be significantly larger than the vortex shedding frequency f_{vs} [32]. On the other hand, too high values would have increased database size unnecessarily. A summary of the number of cells for each mesh along with the ratio between the recurrence sampling frequencies and the shedding frequency f_{vs} is provided in Table 2.

Another matter to consider was the time range of the database τ_{rec} which should cover a suitable number of shedding cycles with period τ_{vs}. In this work, we chose a range of five cycles. The reason for this choice is discussed in detail in Section 4.2.

For generating the recurrence path, we mirrored the databases with respect to the $y = 0$ plane and assigned them equal weights to guarantee symmetric time-averaged results. We chose a mean

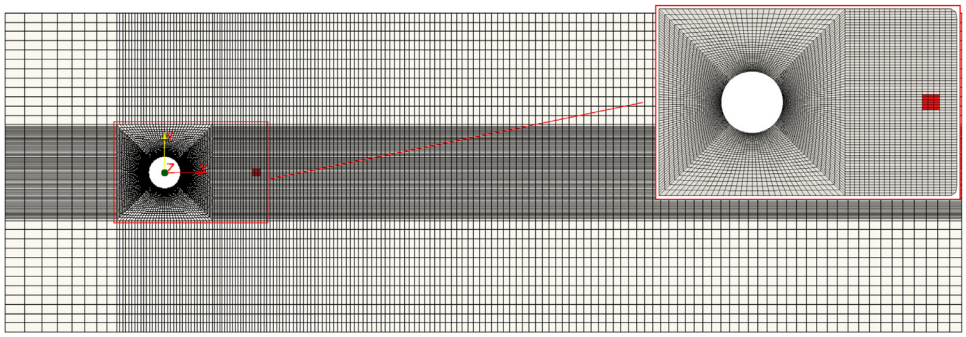

Fig. 4. Illustration of the computational mesh created for rCFD referred to as "R2". The number of the cells is 4.65×10^5. The fine-grid region and the source location are magnified.

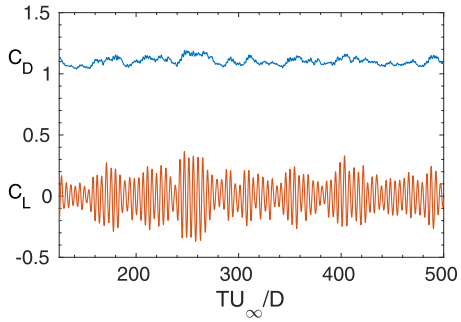

Fig. 5. Time histories of force coefficients of the cylinder at $Re = 3900$. The time range corresponds to approximately 75 vortex shedding cycles. Besides fast oscillations, slower variations are present, too.

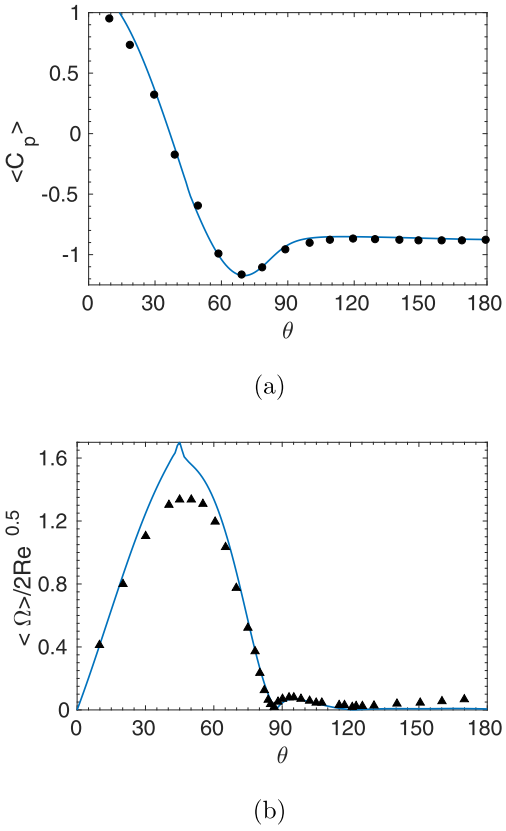

Fig. 6. Wall data for (a) mean pressure coefficient and (b) mean normalized vorticity over the cylinder after 75 shedding cycles at $Re = 3900$. Experimental data are extracted from •: Norberg [65] and ▲: Son and Hanratty [71].

interval size of consecutive fields of $\mathrm{E}(\Delta t/\Delta t_{\mathrm{rec}}) \stackrel{!}{=} 0.2\tau_{\mathrm{rec}}/\Delta t_{\mathrm{rec}}$ from which the corresponding jump probabilities were derived.

Discretization schemes used for rCFD were as the same as the ones in LES, but the generally coarser mesh allowed for a larger time step of $\Delta t_{\mathrm{rCFD}} = 5 \times 10^{-3} D/U_\infty$ for the passive scalar equation.

4. Results

In this section, we present a thorough validation of our LES results and our study on species transport with LES as well as rCFD. The performance improvement by rCFD is highlighted from various perspectives.

4.1. LES results

Varying numbers of shedding periods considered to acquire mean flow statistics can be found in the literature. Franke and Frank [64] mentioned that at least 40 shedding periods are necessary. On the other hand, Lysenko et. al. [60] and D'Alessandro et. al. [61] have gathered statistics over more than 150 shedding cycles for their works. We carried out time averaging over approximately 75 vortex shedding cycles after a duration of $125D/U_\infty$ after which we considered the turbulent flow as fully established.

4.1.1. Wall data

One can define lift and drag coefficients $C_{\mathrm{L}} \equiv F_{\mathrm{L}}/\frac{1}{2}\rho_\infty U_\infty^2 L_z D$ and $C_{\mathrm{D}} \equiv F_{\mathrm{D}}/\frac{1}{2}\rho_\infty U_\infty^2 L_z D$ where F_{L} and F_{D} are normal and tangential forces acting on the cylinder surface, respectively [58]. Fig. 5 depicts time histories of C_{L} and C_{D} over the time range of approximately 75 shedding cycles. We found the root mean square of our lift coefficient, $C_{\mathrm{L,rms}} = 0.13$, is in the range of [0.05,0.6]. Similarly, the mean drag coefficient, $\langle C_{\mathrm{D}} \rangle = 1.1$, is consistent with the results available in literature from both LES and experimental data [60,61,64–69].

The Strouhal number $St \equiv f_{\mathrm{vs}} D/U_\infty$ describes the periodicity of the vortex shedding and can be obtained through fast Fourier transform of the lift coefficient. We determined a value of $St = 0.224$ in close agreement with Zhang et al. [66] and Ouvrard et al. [70].

Fig. 6 a displays the distribution of the time-averaged pressure coefficient $\langle C_{\mathrm{p}} \rangle \equiv 2(\langle p \rangle - p_\infty)/\rho U_\infty$ on the cylinder surface. The resulting mean base suction coefficient of $\left\langle C_{p;\theta=180^\circ} \right\rangle = -0.875$ is in very good agreement with the range $[-0.97, -0.85]$ from other studies [60,61,64,65,68,70].

The normalized magnitude of mean vorticity $\langle \Omega \rangle / 2\sqrt{Re}$ on the cylinder surface, with $\boldsymbol{\Omega} \equiv \nabla \times \bar{\mathbf{u}}$, depicted in Fig. 6b shows a separation angle of $\theta_{\mathrm{sep}} = 87^\circ$ which lies within the bounds $[86^\circ, 89^\circ]$ acquired from experimental and LES data [60,61,64,67,68,71].

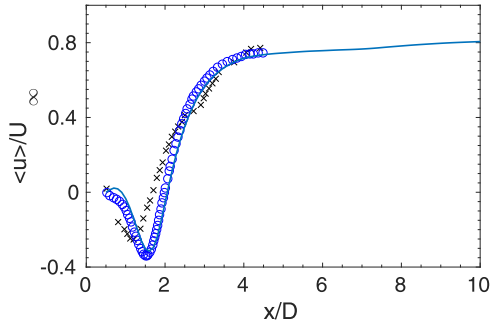

Fig. 7. Mean stream-wise velocity in the wake center-line of the cylinder over approximately 75 shedding cycles at $Re = 3900$. Experimental values were extracted from ○ : Parnaudeau et. al. [59] and × : Lourenco and Shih [67].

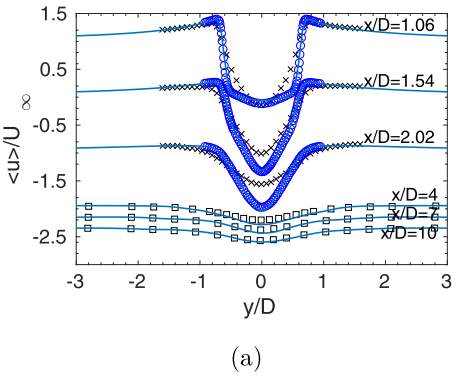

(a)

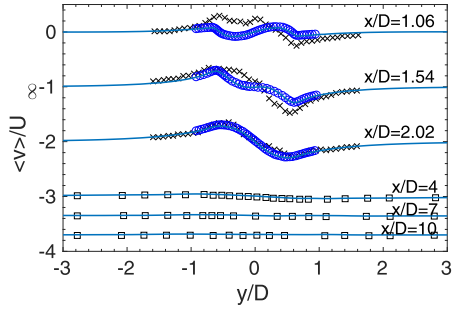

(b)

Fig. 8. Mean (a) stream-wise and (b) transverse velocity at various locations in the wake region of the cylinder over approximately 75 shedding cycles at $Re = 3900$. The values are shifted to plot the velocity profiles all together. — depicts LES results and experimental measurements are sketched from ○ : Parnaudeau et. al. [59], × : Lourenco and Shih [67] and □: Ong and Wallace [72].

4.1.2. Flow statistics

We validated our results for the flow statistics by comparing them with experimental data [59,67]. The time-averaged stream-wise velocity component along the center-line of the wake region presented in Fig. 7 is in excellent agreement with the work of Parnaudeau et al. [59]. Fig. 8 illustrates the mean velocity profiles at different sections in the wake of the cylinder compared to measurements. Likewise, mean velocity fluctuations are sketched along with the experimental information in Fig. 9. It is evident that the present simulation was very close to the PIV measurements [59].

Table 3 provides a summary of our LES data compared to other studies.

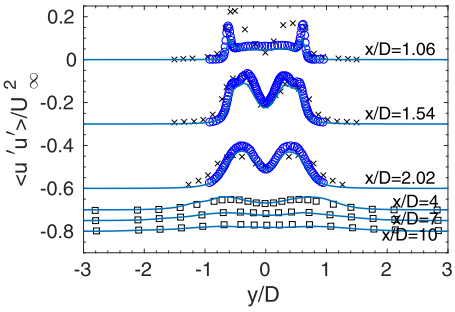

(a)

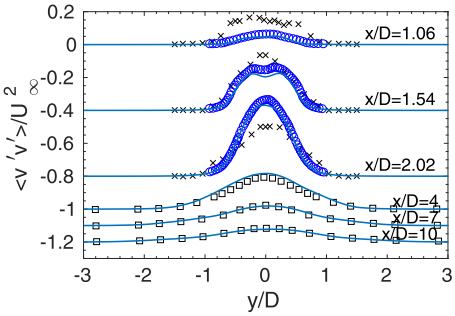

(b)

Fig. 9. Mean (a) stream-wise and (b) transverse velocity fluctuations. For details refer to the caption for Fig. 8.

Table 3
Integral flow features. An overview of both experimental and numerical studies is presented.

	$C_{l,rms}$	C_d	L_r/D	θ_{sep}	$-\langle C_{p,b}\rangle$
Parnaudeau et al. [59]	–	–	1.51	–	–
Lourenco and Shih [67]	–	0.99	1.18	–	–
Kravchenko and Moin [68]	–	1.04	1.35	88°	0.94
Lysenko et al. [60]	0.09	0.97	1.67	88°	0.91
D'Alessandro et al. [61]	0.146	1.023	1.427	87°	0.878
Norberg [65]	0.15	0.98	–	–	0.90
this work	0.13	1.1	1.55	87°	0.875

4.2. Recurrence analysis

The rCFD procedure relies on a database of adequate size which is generally not known a priori. Since both its creation and manipulation are computationally expensive, one will look for it to be as small as possible but still contain the relevant physics of the flow it was obtained from. If any symmetries of the system are known, one can use them to extend it with hardly any additional costs. Therefore, we expanded the database containing approximately five shedding cycles (see below for the choice of size) with velocity fields mirrored in y-direction as explained in Section 3.

Next, we assessed the flow's degree of recurrence after the cylinder by calculating the distance norms for both databases to obtain the combined one, $D(t, t')$, shown in Fig. 10 for R2 with $\Delta t_{rec}/\Delta t_{LES} = 50$. One can intuitively perceive some amount of periodicity corresponding to τ_{vs}. Line plots of $D(t, t')$ with one time argument fixed in Fig. 11 underline that while minima are located at multiples of τ_{vs}, the flow is clearly not fully periodic. Although velocity fields recur approximately after τ_{vs}, they are not identical due to turbulent fluctuations. This explains the need to retain several shedding cycles for a proper description.

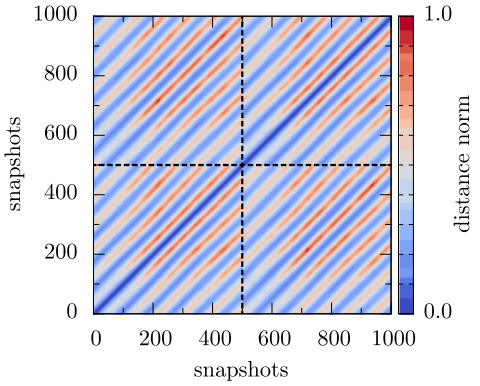

Fig. 10. The combined distance plot calculated for R2 corresponding to $\tau_{rec} = 10$ shedding cycles. The dashed line separates the primary database and the mirrored one. Parallel to the main diagonal, weaker local minima (similar configurations) are located, which are separated by pronounced maxima (different states).

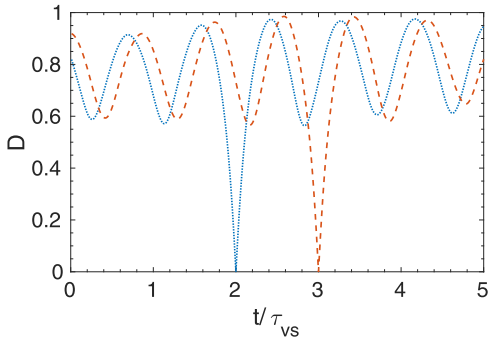

Fig. 11. The distance norm value for R2 at the times of 2 (——) and 3 (– – –) cycles for the primary database. Though recurrent within a certain tolerance, the flow is not fully periodic.

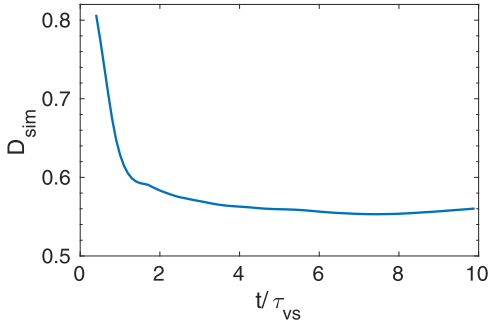

Fig. 12. Average nearest-neighbor distance over recurrence matrix size. After a fast drop, the curve decreases slowly and even shows a very weak increment for large times. For each duration, the recurrence matrix contained the same number of original and of mirrored flow fields.

We stress that such a (pseudo-)periodicity is not necessary for rCFD which can handle a completely irregular reappearance of patterns as long as the database contains their recurrence.Consequently, the average degree of recurrence may be used as an indicator for sufficient database size by looking at the evolution of the mean nearest neighbor distance $D_{sim}(t)$ defined in Eq. (19). In a recent study on a gas-solid fluidized bed, one of us [73] found a pronounced initial drop of $D_{sim}(t)$ that was followed by a slow descent connected to the complexity of the system. Once within the second regime which may even show slight, temporary increments of $D_{sim}(t)$, extending the database added only little further information. Fig. 12 illustrates $D_{sim}(t)$ for the combined, i.e. symmetrized, database for up to ten cycles. Unsurprisingly, the characteristic, fast drop is followed by a rather constant plateau after one to two shedding cycles. After this duration, new information accumulates only slowly. As a compromise between memory demands and sufficient amounts of information, we generally use database sizes of a few multiples of the dropping time as a rule of thumb. In the present case, we chose approximately five cycles, which resulted in a total of ten cycles because of the symmetrization procedure.

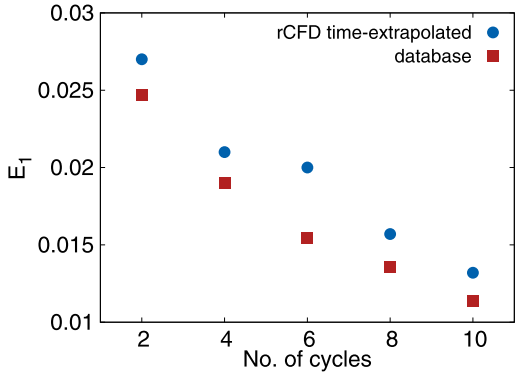

(a)

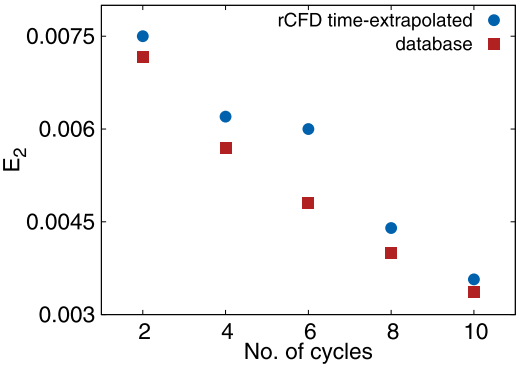

(b)

Fig. 13. Comparison of error norms for (a) time-averaged velocity and (b) its fluctuation over 75 shedding cycles with different numbers of shedding cycles in the database. A clear trend of decreasing errors with database size can be observed. Each database contained symmetrized velocity fields, e.g. two cycles consisted of one recorded cycle plus its mirrored counterpart. Note that for velocity, the error obtained from the mean and variance of the database was generally lower than that from the recurrence process (see text for more details).

4.3. Time-extrapolation

Using the recurrence database, we could time-extrapolate the evolution of $\mathbf{u}(\mathbf{r}, t)$. In order to verify if the recording duration based on $D_{sim}(t)$ had been sufficiently long to reproduce statistically valid long-term properties, we investigated the time-averaged velocity components and its fluctuations over 75 shedding cycles acquired from rCFD simulations with different numbers of cycles in the database and compared them with mean profiles calculated from the database itself according to different number of shedding cycles. Therefore, we defined error norms

$$E_1 = \frac{1}{VU_\infty} \int d^3r |\bar{\mathbf{u}} - \bar{\mathbf{u}}_{\mathrm{LES}}| \tag{28}$$

$$E_2 = \frac{1}{VU_\infty^2} \int d^3r |\overline{u'u'} - \overline{u'u'}_{\mathrm{LES}}| \tag{29}$$

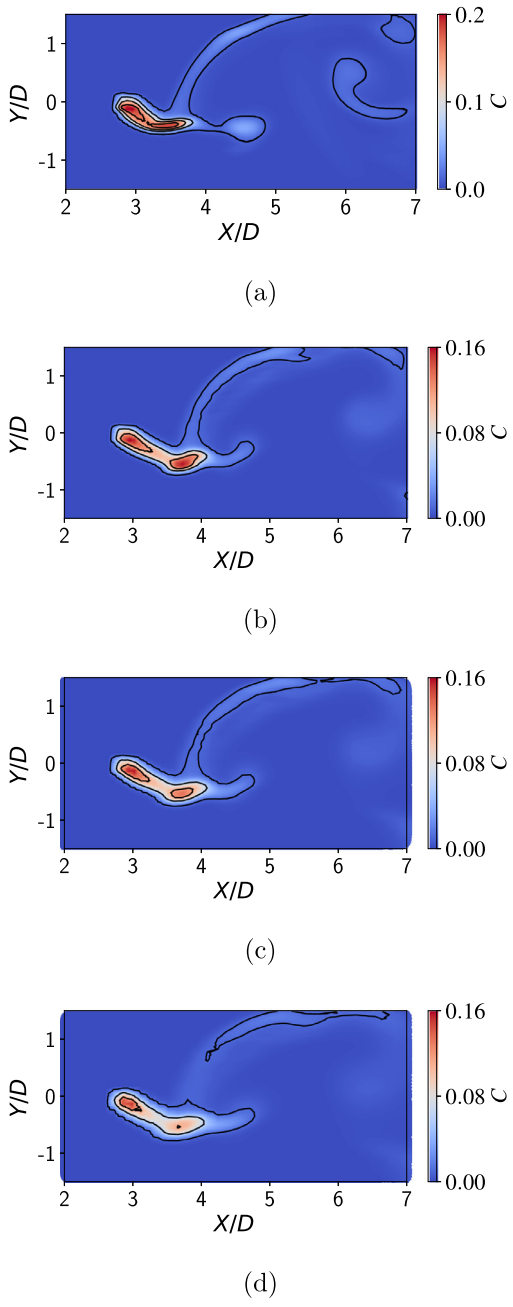

Fig. 14. Snapshots of species concentration at $t = 3\tau_{rec}$ for (a) LES on L1 and rCFD on (b) R1, (c) R2 and (d) R3. The effect of grid coarsening can be observed. Contour lines are sketched at values of 0.01, 0.06, 0.11, 0.13.

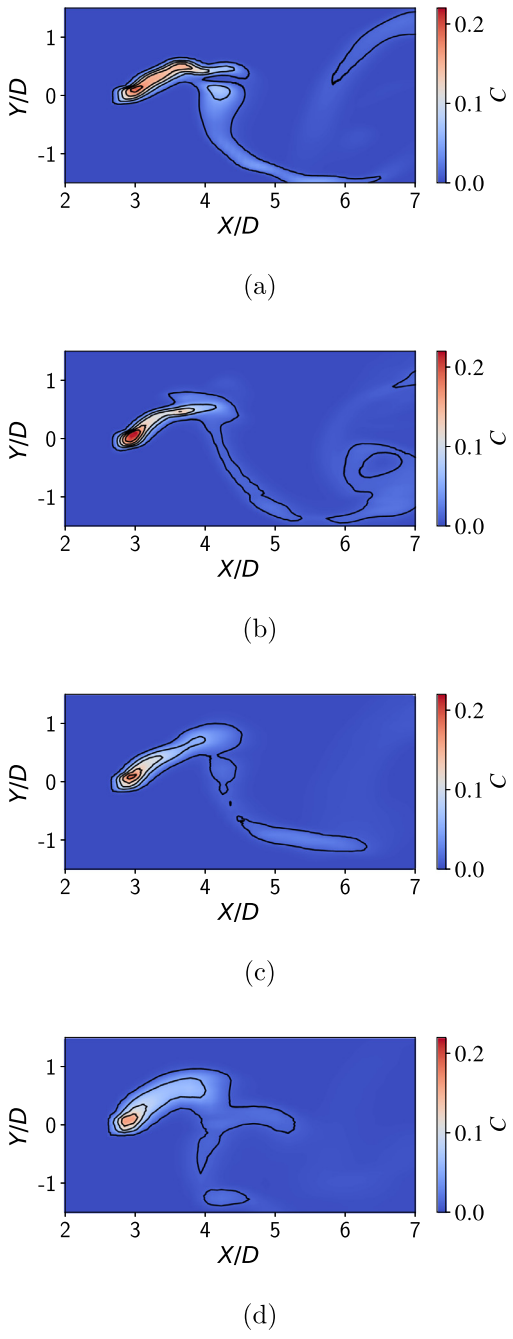

Fig. 15. Snapshots of species concentration at $t = 30\tau_{rec}$ for (a) LES on L1 and rCFD on (b) R1, (c) R2 and (d) R3. Due to turbulent fluctuations and the approximate nature of the recurrence process, single realizations can differ, but are accurate in a statistical sense. Contour lines are sketched at values of 0.01, 0.05, 0.09, 0.13 and 0.17.

which are displayed in Fig. 13. The errors from the recurrence process after a few shedding cycles were in the range of one or two percent and below for the velocity average and fluctuations, respectively, which we deemed acceptable for our purposes. Interestingly, the errors kept decreasing when the mean recurrence degree in Fig. 12 had already leveled out. Consequently, one should not blindly rely on a single characteristic number of the recurrence statistics, but carry out a posteriori analyses, too.

Additionally, we underline the purpose of rCFD to study long-term processes like species transport by time-extrapolating the underlying velocity field. However, it does not provide new information on velocity itself. Hence, the error in the time-extrapolated velocity field cannot be lower than that of the evenly time-averaged database in Fig. 13. We stress that the situation is utterly different for species transport (cf. Section 4.4).

4.4. Species transport

We studied passive scalar transport by adding a source in the wake region (cf. Fig. 3). Instantaneous mass concentrations in the wake region at two selected times for LES on L1 and rCFD on R1, R2 and R3 are displayed in Figs. 14 and 15. In the beginning of the rCFD simulations, the generated recurrence paths were the same, therefore species profiles demonstrated similar patterns at $t = 3\tau_{vs}$. After some time at $t = 30\tau_{vs}$ with arising slight changes

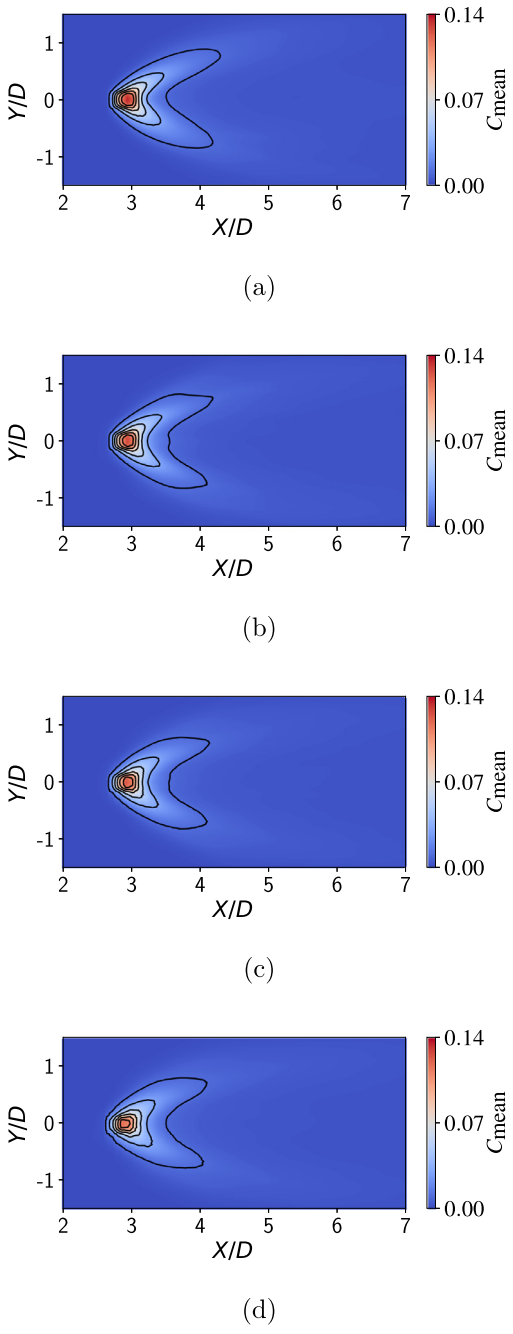

Fig. 16. Snapshots of mean species after 75 cycles for (a) LES on L1 and rCFD on (b) R1, (c) R2 and (d) R3. Contour lines are sketched at values of 0.01, 0.03, 0.05, 0.07, 0.09 and 0.11.

in recurrence paths in each rCFD simulation and depending on the level of fluctuations in these periods, the instantaneous profiles showed some minor deviations particularly further downstream of the source. However, the time-averaged species profiles after 75 shedding cycles presented in Fig. 16 agreed extremely well and different recurrence paths did not affect the mean species profile due to statistical averaging. Fig. 17 compares time-averaged concentration profiles over 5 and 75 shedding cycles and verifies the necessity of time averaging over long time periods (as mentioned in Section 4.1) in order to acquire statistically valid data for turbulent flows.

We note that the results for the first two grids were in very good agreement with the LES simulation with reduced cell numbers by factors of 5 and 8, and even the coarsest mesh with 1/15 of the original cell number showed only little deviations. The effect of grid coarsening could be distinguished for time-averaged species fluctuations in Fig. 18. However, one can observe that the profiles were qualitatively comparable.

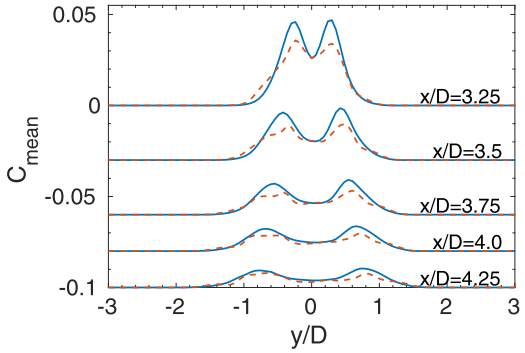

Fig. 17. Time-averaged species transport profile at different locations in the wake region of the cylinder over _ _ _ : 5 and ▬: 75 shedding cycles. A large number of shedding cycles is required for statistical averaging because of the high-level of fluctuations. The data are shifted to be visible in one plot.

Table 4
The relative error for the time-averaged, total amount of species in the whole domain.

Mesh	Relative error
R1	0.0064
R2	0.0066
R3	0.007

For the sake of a more detailed comparison, we provide three groups of species line plots based on different values of Δt_{rec} for the computational grids specified in Table 2. Fig. 19a illustrates the mean profiles at different sections in the wake region of the cylinder studied with LES on L1 compared to rCFD on R1, R2 and R3 with the smallest Δt_{rec}. rCFD on R1 and R2 was in very good agreement with LES, but for the coarsest mesh R3, we see the onset of deviations. The same behavior can be observed for larger time steps, i.e. smaller recurrence frequencies in Fig. 19b and c, which indicates that one may be quite generous with the choice of sampling steps.

Additionally, we provide two quantitative measures for the obtained accuracy. The relative error for the system-wide, total amount of time-averaged species calculated from rCFD on R1, R2 and R3 in comparison to LES on L1 was well below one percent for all investigated cases, cf. Table 4. Furthermore, the error

$$E_{\text{C}} = \int d^3r |\bar{C} - \bar{C}_{\text{LES}}| \tag{30}$$

of the spatial species distribution is displayed in Fig. 20 for the various meshes. Although the number of cells was decreased 5, 8 and 15 times, the error remained in the same order of magnitude, which demonstrates that rCFD is capable of dealing with rather coarse grids. However, we believe that an intuitive notion for the method's accuracy may be drawn more easily from Figs. 14–19.

Furthermore, Fig. 21 shows a comparison between the errors of species distribution time-averaged over 75 shedding cycles from rCFD and obtained from considering only databases with different number of cycles without extrapolation. Here, one can observe the importance of methods like rCFD since even for an almost periodic process like vortex shedding and even after 10 cycles, it makes a difference for species profiles if we time-extrapolate the dynamics or not.

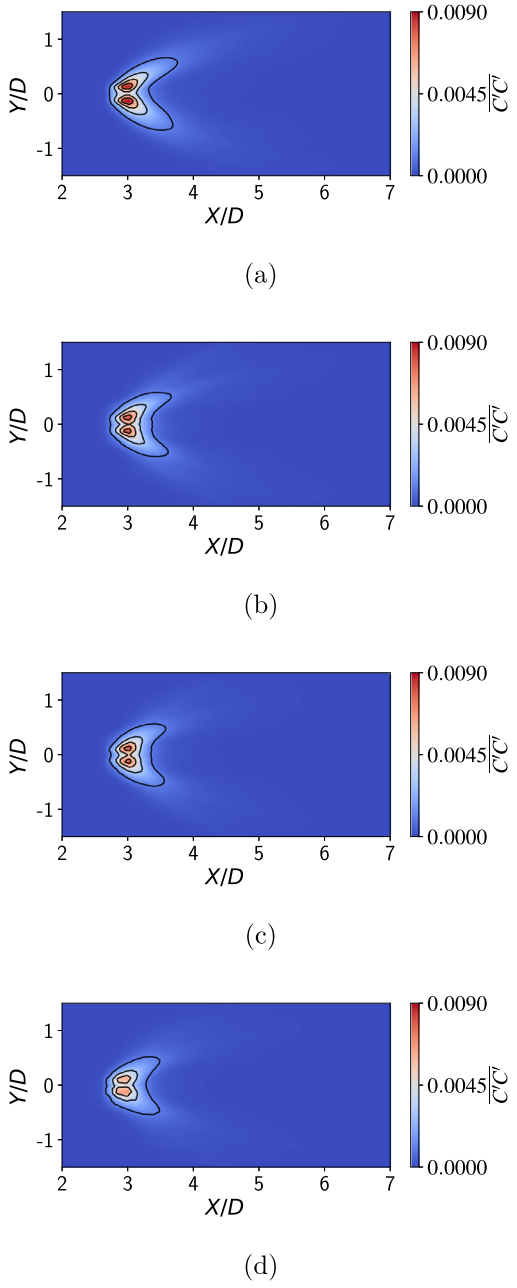

Fig. 18. Snapshots of mean species fluctuations after 75 cycles for (a) LES on L1 and rCFD on (b) R1, (c) R2 and (d) R3. Contour lines are sketched at values of 0.001, 0.003, 0.005 and 0.007.

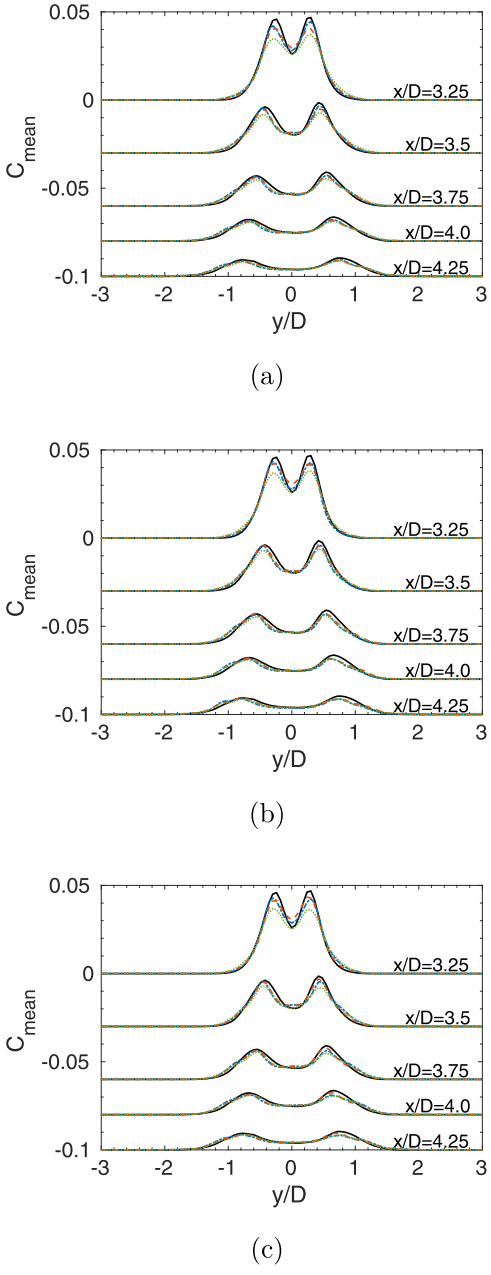

Fig. 19. Mean mass transport profile at different locations in the wake region of the cylinder at $Re = 3900$ for the recurrence time intervals of (a) $\Delta t_{rec}/\Delta t_{LES} = 10$, (b) $\Delta t_{rec}/\Delta t_{LES} = 50$ and (c) $\Delta t_{rec}/\Delta t_{LES} = 100$. — corresponds to LES on L1, -.- to rCFD on R1, _ _ _ rCFD on R2 and ... rCFD on R3. The data are shifted to be visible in one plot.

The resilience of rCFD towards grid coarsening is underlined by the anticipated, unsatisfactory performance of LES on equally coarse meshes. We carried out an LES on R1 and compare time-averaged species profiles on L1 and R1 over 75 shedding cycles in Fig. 22. As expected, without very fine grids and small time steps (associated with much higher computational costs), LES led to poor results, while rCFD worked well with a considerably reduced number of cells as well as greater time steps.

4.5. Performance analysis

One of the main purposes and advantages of the rCFD method is the reduction of computational costs. We analyzed its performance for turbulent vortex shedding for various selected cases specified in Table 5. To draw a reasonable comparison, we tried to keep the number of cells per number of processors approximately constant. Therefore, the last column of Table 5 corresponds to number of cells per one core.

Fig. 23 depicts the total run-time of the LES and rCFD cases separated into contributions from the solution of the passive scalar transport equation and from other processes. The drastic reduction of the overall computation time had two reasons. First, about 90% of run-time in LES was spent with the velocity and pressure equations which need not to be solved in rCFD. Second, due to the larger permissible value of Δt_{rCFD} compared to Δt_{LES}, the passive transport equation was solved more than 14 times faster in rCFD than in LES.

On the other hand, rCFD had to read the database and calculate the distance matrix, for which the loading time is presented in

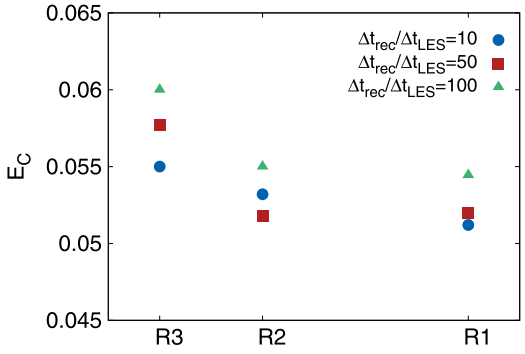

Fig. 20. The error E_C of the spatial species distribution for different grid resolutions. The resilience of rCFD towards mesh coarsening can be deduced from the relatively weak dependence of E_C from the cell number.

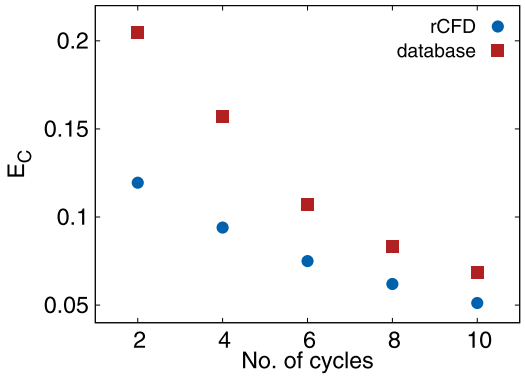

Fig. 21. The error E_C of the spatial species distribution for different number of cycles in the database. The difference of 1.5% even after 10 shedding cycles demonstrates the advantage of using rCFD.

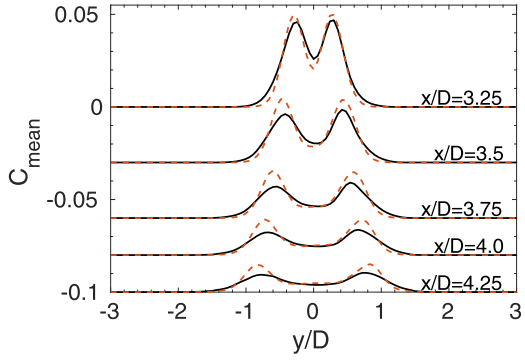

Fig. 22. Normalized mean mass transport at different locations in the wake region of the cylinder at $Re = 3900$ performed by LES on L1 and R1. — corresponds to LES for L1 and _ _ _ to LES for R1. As expected, LES becomes inaccurate with coarser grids. The data are shifted to be visible in one plot.

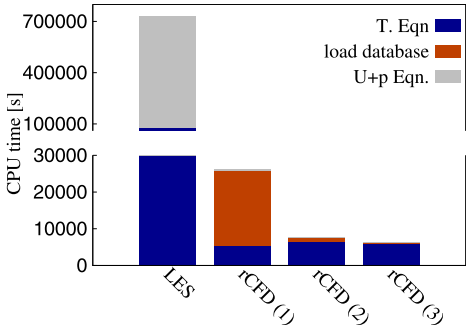

Fig. 23. CPU times for LES and rCFD cases with the details explained in Table 5. CPU times for different grids with the same recurrence time interval in rCFD approach are approximately in the same order of magnitude.

Table 5
Details of each case for the performance analysis. The number of cells per processor is mentioned to provide a comparison.

Case	Mesh	Δt_{rec}	No. of processors	No. of cells / core
LES	L1	–	40	96 125
rCFD(1)	R1	$10 \times \Delta t_{LES}$	8	96 000
rCFD(2)	R2	$50 \times \Delta t_{LES}$	4	118 750
rCFD(3)	R3	$100 \times \Delta t_{LES}$	2	132 500

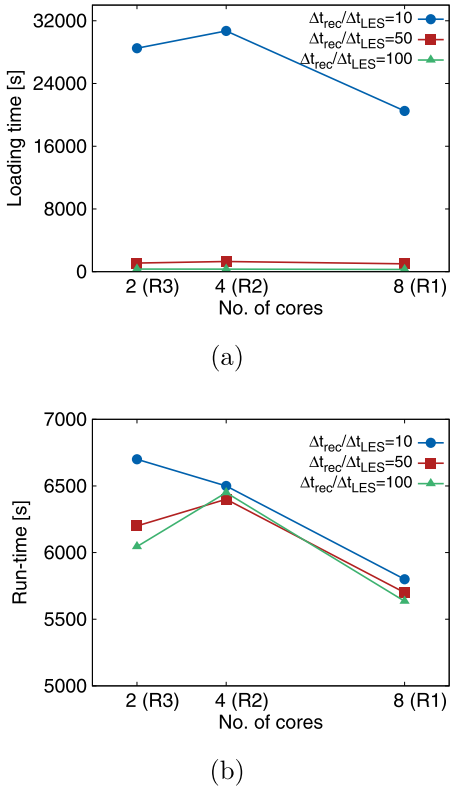

Fig. 24. (a) Loading and (b) simulation times for different grids with various sampling time steps Δt_{rec} carried out by rCFD. Due to the number of cells per CPU, results are rather insensitive to the number of cores. Loading times show a very high dependence on Δt_{rec}, while simulation run-times are less affected.

Fig. 24a. By increasing the sampling time step, the number of snapshots in the database decreased, and therefore the loading time for our largest recurrence time step was reduced by at least one order of magnitude. While it constituted the major contribution to run-time for the case with the smallest sampling step, it became negligible for that with the largest one.

CPU times for updating the fields along with solving the passive transport equation are indicated in Fig. 24b. The simulation times were close to each other because we used approximately the same number of cells per processor. We note that the lower simulation time for R1 corresponds to the lower number of cells per one CPU in comparison to other grids.

Altogether, the LES simulation was performed on 40 processors with an approximate total time of 200 h while our rCFD simulation on the coarsest mesh and with the largest sampling step took only about 6000 sec on 2 processors. This amounts in a speed-up of more than 120 at 1/20 of required CPU power.

As mentioned above, since finer grids increase loading and hence total run-time, we recommend to use as coarse meshes as compatible with the resolution of the meso- and macroscopic phenomena of interest. Furthermore, they are much less demanding with regard to memory consumption than geometries with huge

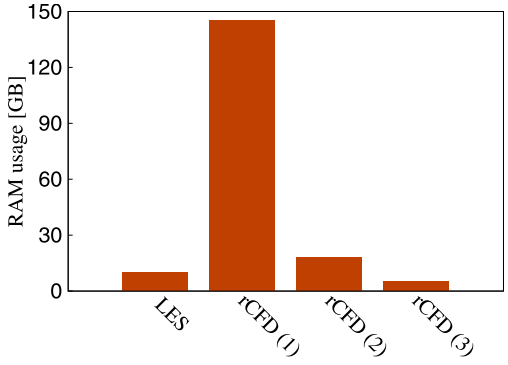

Fig. 25. RAM usage for LES and rCFD cases. Too fine meshes and small sampling steps cause an excessive memory consumption of rCFD. Details are provided in Table 5.

cell numbers as illustrated in Fig. 25. In such cases, RAM could easily become the limiting factor.

5. Conclusion and outlook

In this work, we have demonstrated the application of rCFD to species transport in the turbulent flow after a circular cylinder at $Re = 3900$ and compared it with a detailed LES which we validated against experimental and numerical data. The good agreement of time-resolved and -averaged species profiles between rCFD and LES shows that already short time series of the velocity field contain most of the relevant information required for long-term studies if reappearing patterns prevail and smallest-scale structures are not of interest. We stress that recurrences within some tolerance (which will ultimately affect the obtained accuracy) are sufficient and no strict periodicity is needed, which would make the whole procedure trivial. Elsewhere [74], one of us demonstrated that not even a clearly dominating frequency as f_{vs} is necessary to construct a proper recurrence process.

The obtained speed-ups of more than 120 at 1/20 of the required computer power originated from various sources. Most importantly, rCFD only solves the passive transport equation but neither that for velocity nor that for pressure. Consequently, meshes may be much coarser and time steps larger than for LES. More specifically, we employed three different computational grids with 5, 8 and 15 times less cells as well as a time step 5 times greater than for LES. The database loading time and memory consumption of rCFD, which could have otherwise easily become bottlenecks, were reduced by increasing the sampling time step and lowering spatial resolution, respectively.

Since we used a relatively simple, idealized test case for our novel method, there are several open questions and tasks for future investigations. Among various others, we stress two current restrictions. Firstly, similarity of states depends on the underlying norm which is chosen quite subjectively. In the case of transport in single-phase flow, it is reasonable to compare velocity fields with each other, but the situation becomes more complicated for multiple phases. Is velocity alone still a good indicator or should one rather contrast local volume fractions or combinations thereof? Secondly, we considered completely passive species transport that did not affect the velocity field. However, many slow, long-lasting processes alter the fluid dynamics gradually or abruptly. Heat transfer or chemical conversion can change density or viscosity, which in turn will impact the flow. For such scenarios, it will be necessary to create more than a single database corresponding to different parameter settings and interpolate between them [51].

In summary, we can state that rCFD significantly reduced the computational costs for the investigated case. For the finer two grids, the results agreed very well with the full simulation, and only for the coarsest mesh, we found slight differences, which we regard as an indicator for the lower resolution limit of our simulation. Taken all together, this makes us optimistic that rCFD can be a useful method for fast long-term studies of turbulent flows. We are convinced that eventually, it will be applicable not only to passive, single-phase but to coupled, multi-phase problems.

Declaration of Competing Interest

The authors declare that they have no known competing financial interests or personal relationships that could have appeared to influence the work reported in this paper.

Acknowledgement

This work was partly funded by the Linz Institute of Technology (LIT), Johannes Kepler University (project LIT-2016-1-YOU-007). We furthermore acknowledge support from K1-MET GmbH metallurgical competence center.

References

[1] Pope S. Modeling and Simulation. Cambridge, UK: Cambridge Univ. Press; 2000.
[2] Orszag SA, Patterson GS. Numerical simulation of three-dimensional homogeneous isotropic turbulence. Phys Rev Lett 1972;28:76–9.
[3] Rogallo RS. Numerical experiments in homogeneous turbulence. NASA Technical Report TM-81315; 1981.
[4] Moin P, Mahesh K. Direct numerical simulation: a tool in turbulence research. Annu Rev Fluid Mech 1998;30(1):539–78.
[5] Leonard A. Energy cascade in large-eddy simulations of turbulent fluid flows. In: Frenkiel F, Munn R, editors. Turbulent diffusion in environmental pollution. Adv. Geophys., vol. 18. Elsevier; 1975. p. 237–48.
[6] Reynolds O. On the dynamical theory of incompressible viscous fluids and the determination of the criterion. Proc Roy Soc A 1894;451(1941):5–47.
[7] Liepmann HW. Aspects of the turbulence problem. Z Angew Math Phys 1952;3(6):407–26.
[8] Townsend AA. The structure of turbulent shear flow. Cambridge, UK: Cambridge Univ. Press; 1980.
[9] Liu J. Contributions to the understanding of large-scale coherent structures in developing free turbulent shear flows. Adv Appl Mech 1988;26:183–309.
[10] Berkooz G, Holmes P, Lumley JL. The proper orthogonal decomposition in the analysis of turbulent flows. Annu Rev Fluid Mech 1993;25(1):539–75.
[11] Taira K, Brunton SL, Dawson ST, Rowley CW, Colonius T, McKeon BJ, et al. Modal analysis of fluid flows: an overview. AIAA J 2017:4013–41.
[12] Holgate J, Skillen A, Craft T, Revell A. A review of embedded large eddy simulation for internal flows. Arch Comput Method E 2018;139:1–18.
[13] Long X, Cheng H, Ji B, Arndt RE, Peng X. Large eddy simulation and Euler-Lagrangian coupling investigation of the transient cavitating turbulent flow around a twisted hydrofoil. Int J Multiphas Flow 2018;100:41–56.
[14] Mathur A, Seddighi M, He S. Transition of transient channel flow with high Reynolds number ratios. Entropy 2018;20(5):257–89.
[15] Qi Y, Ishihara T. Numerical study of turbulent flow fields around of a row of trees and an isolated building by using modified k-ε model and LES model. J Wind Eng Ind Aerod 2018;177:293–305.
[16] Tunstall R, Laurence D, Prosser R, Skillen A. Towards a generalised dual-mesh hybrid LES/RANS framework with improved consistency. Comput Fluids 2017;157:73–83.
[17] Thé J, Yu H. A critical review on the simulations of wind turbine aerodynamics focusing on hybrid RANS-LES methods. Energy 2017;138:257–89.
[18] Cazemier W, Verstappen R, Veldman A. Proper orthogonal decomposition and low-dimensional models for driven cavity flows. Phys Fluids 1998;10(7):1685–99.
[19] Iollo A, Lanteri S, Désidéri J-A. Stability properties of POD–Galerkin approximations for the compressible Navier–Stokes equations. Theor Comput Fluid Dyn 2000;13(6):377–96.
[20] Sirisup S, Karniadakis G. A spectral viscosity method for correcting the long-term behavior of POD models. J Comput Phys 2004;194(1):92–116.
[21] Sirisup S, Karniadakis G. Stability and accuracy of periodic flow solutions obtained by a POD-penalty method. Physica D 2005;202(3-4):218–37.
[22] Sirisup S, Karniadakis G, Xiu D, Kevrekidis I. Equation-free/Galerkin-free POD-assisted computation of incompressible flows. J Comput Phys 2005;207(2):568–87.
[23] Akhtar I, Nayfeh AH, Ribbens CJ. On the stability and extension of reduced-order Galerkin models in incompressible flows. Theor Comput Fluid Dyn 2009;23(3):213–37.

[24] Bergmann M, Bruneau C-H, Iollo A. Enablers for robust POD models. J Comput Phys 2009;228(2):516–38.
[25] Fick L, Maday Y, Patera AT, Taddei T. A stabilized POD model for turbulent flows over a range of Reynolds numbers: Optimal parameter sampling and constrained projection. J. Comput. Phys. 2018;371:214–43. doi:10.1016/j.jcp.2018.05.027.
[26] Rozza G, Veroy K. On the stability of the reduced basis method for Stokes equations in parametrized domains. Comput Methods Appl Mech Eng 2007;196(7):1244–60.
[27] Gerner A-L, Veroy K. Certified reduced basis methods for parametrized saddle point problems. SIAM J Sci Comput 2012;34(5):A2812–36.
[28] Rozza G, Huynh DP, Manzoni A. Reduced basis approximation and a posteriori error estimation for stokes flows in parametrized geometries: roles of the inf-sup stability constants. Numer Math 2013;125(1):115–52.
[29] Caiazzo A, Iliescu T, John V, Schyschlowa S. A numerical investigation of velocity–pressure reduced order models for incompressible flows. J Comput Phys 2014;259:598–616.
[30] Ballarin F, Manzoni A, Quarteroni A, Rozza G. Supremizer stabilization of POD–Galerkin approximation of parametrized steady incompressible Navier–Stokes equations. Int J Numer Methods Eng 2015;102(5):1136–61.
[31] Stabile G, Rozza G. Finite volume POD-Galerkin stabilised reduced order methods for the parametrised incompressible Navier–Stokes equations. Comput Fluids 2018;173:273–84.
[32] Lichtenegger T, Pirker S. Recurrence CFD - a novel approach to simulate multiphase flows with strongly separated time scales. Chem Eng Sci 2016;153:394–410.
[33] Eckmann J, Kamphorst S, Ruelle D. Recurrence plots of dynamical systems. Europhys Lett 1987;4(9):973–7.
[34] Zbilut JP, Webber CL. Embeddings and delays as derived from quantification of recurrence plots. Phys Lett A 1992;171(3):199–203.
[35] Webber CL, Zbilut JP. Dynamical assessment of physiological systems and states using recurrence plot strategies. J Appl Physiol 1994;76(2):965–73.
[36] Cecconi F, Cencini M, Falcioni M, Vulpiani A. Predicting the future from the past: an old problem from a modern perspective. Am J Phys 2012;80(11):1001–8.
[37] Smagorinsky J. General circulation experiments with the primitive equations. Mon Weather Rev 1963;91:99–164.
[38] Daly BJ, Harlow FH. Transport equations in turbulence. Phys Fluids 1970;13(11):2634–49.
[39] Abe K, Suga K. Towards the development of a Reynolds-averaged algebraic turbulent scalar-flux model. Int J Heat Fluid Flow 2001;22(1):19–29.
[40] Combest D, Ramachandran P, Dudukovic M. On the gradient diffusion hypothesis and passive scalar transport in turbulent flows. Ind Eng Chem Res 2011;50(15):8817–23.
[41] Ryan K, Bodart J, Folkersma M, Elkins C, Eaton J. Turbulent scalar mixing in a skewed jet in crossflow: experiments and modeling. Flow Turbul Combust 2017;98(3):781–801.
[42] Nilsen KM, Kong B, Fox RO, Hill JC, Olsen MG. Effect of inlet conditions on the accuracy of large eddy simulations of a turbulent rectangular wake. Chem Eng J 2014;250:175–89.
[43] Jansen K, Kong B, Fox R, Hill J, Olsen M. Large eddy simulation of passive scalar transport in a high Schmidt number turbulent incompressible wake with experimental validation. Chem Eng Sci 2015;137:862–74.
[44] Karakasidis TE, Liakopoulos A, Fragkou A, Papanicolaou P. Recurrence quantification analysis of temperature fluctuations in a horizontal round heated turbulent jet. Int J Bifur Chaos 2009;19(08):2487–98.
[45] Guimarães-Filho ZdO, Caldas IL, Viana RL, Nascimento IC, Kuznetsov YK, Kurths J. Recurrence quantification analysis of turbulent fluctuations in the plasma edge of Tokamak Chauffage Alfvén Brésilien tokamak. Phys Plasmas 2010;17(1):012303.
[46] Lardeau S, Tessicini F, Leschziner MA. Analysis of cyclic events in turbulent flows using recurrence plots. J Turbul 2010(11):N16.
[47] Mukherjee S, Zawar-Reza P, Sturman A, Mittal AK. Characterizing atmospheric surface layer turbulence using chaotic return map analysis. Meteorol Atmos Phys 2013;122(3-4):185–97.
[48] Tahmasebpour M, Zarghami R, Sotudeh-Gharebagh R, Mostoufi N. Study of transition velocity from bubbling to turbulent fluidisation by recurrence plots analysis on pressure fluctuations. Can J Chem Eng 2013;91(2):368–75.
[49] Górski G, Litak G, Mosdorf R, Rysak A. Two phase flow bifurcation due to turbulence: transition from slugs to bubbles. Eur Phys J B 2015;88(9):239.
[50] Suresha S, Sujith R, Emerson B, Lieuwen T. Nonlinear dynamics and intermittency in a turbulent reacting wake with density ratio as bifurcation parameter. Phys Rev E 2016;94(4):042206.
[51] Pirker S, Lichtenegger T. Process control of through-flow reactor operation by real-time recurrence CFD (rCFD) simulations - proof of concept. Chem Eng Sci 2019;198:241–52.
[52] Lichtenegger T, Kieckhefen P, Heinrich S, Pirker S. Dynamics and long-time behavior of gas-solid flows on recurrent-transient backgrounds. Chem Eng J 2019;364:241–52.
[53] Germano M, Piomelli U, Moin P, Cabot W. A dynamic subgrid scale eddy viscosity model. Phys Fluids A 1991;3(7):1760–5.
[54] Germano M. Turbulence: the filtering approach. J Fluid Mech 1992;238:325–36.
[55] Stolz S, Adams NA. An approximate deconvolution procedure for large-eddy simulation. Phys Fluids 1999;11(7):1699–701.
[56] Nikolaou ZM, Vervisch L. A priori assessment of an iterative deconvolution method for LES sub-grid scale variance modelling. Flow Turbul Combust 2018;101(1):33–53.
[57] Davidson P. The ubiquitous nature of turbulence. Oxford, UK: Oxford Univ. Press; 2004.
[58] Beaudan P, Moin P. Numerical experiments on the flow past a circular cylinder at sub-critical Reynolds number. NASA STI/Recon Technical Report TF-62; 1994.
[59] Parnaudeau P, Carlier J, Heltz D, Lamballais E. Experimental and numerical studies of the flow over a circular cylinder at Reynolds number 3900. Phys Fluids 2008;20(8):085–101.
[60] Lysenko D, Ertesvåg I, Rian K. Large-eddy simulation of the flow over a circular cylinder at Reynolds number 3900 using the OpenFOAM toolbox. Flow Turbul Combust 2012;89(4):491–518.
[61] D'Alessandro V, Montelpare S, Ricci R. Detached-eddy simulations of the flow over a cylinder at Re = 3900 using OpenFOAM. Comput Fluids 2016;136:152–69.
[62] Issa RI. Solution of the implicitly discretised fluid flow equations by operator-splitting. J Comput Phys 1986;62(1):40–65.
[63] Versteeg H, Malalasekera W. An introduction to computational fluid dynamics: the finite volume method. Harlow, UK: Pearson Education Limited; 1995.
[64] Franke J, Frank W. Large eddy simulation of the flow past a circular cylinder at $Re_d = 3900$. J Wind Eng Ind Aerod 2002;90(10):1191–206.
[65] Norberg C. An experimental investigation of the flow around a circular cylinder: influence of aspect ratio. J Fluid Mech 1994;258:287–316.
[66] Zhang H, Yang J, Xiao L, Lü H. Large-eddy simulation of the flow past both finite and infinite circular cylinders at Re = 3900. J Hydrodyn Ser B 2015;27(2):195–203.
[67] Lourenco L., Shih C.. Characteristics of the plane turbulent near wake of a circular cylinder. A particle image velocimetry study. Published in Ref[68]1993;.
[68] Kravchenko A, Moin P. Numerical studies of flow over a circular cylinder at $Re_d = 3900$. Phys Fluids 2000;12(2):403–17.
[69] Pereira F, Vaz G, Eça L, Girimaji S. Simulation of the flow around a circular cylinder at Re=3900 with partially–averaged Navier–Stokes equations. Int J Heat Fluid Flow 2018;69:234–46.
[70] Ouvrard H, Koobus B, Dervieux A, Salvetti M. Classical and variational multiscale LES of the flow around a circular cylinder on unstructured grids. Comput Fluids 2010;39(7):1083–94.
[71] Son JS, Hanratty TJ. Velocity gradients at the wall for flow around a cylinder at Reynolds numbers from 5×10^3 to 10^5. J Fluid Mech 1969;35(2):353–68.
[72] Ong L, Wallace J. The velocity field of the turbulent very near wake of a circular cylinder. Exp Fluids 1996;20(6):441–53.
[73] Lichtenegger T. Local and global recurrences in dynamic gas-solid flows. Int J Multiphas Flow 2018;106:125–37.
[74] Lichtenegger T, Peters E, Kuipers J, Pirker S. A recurrence CFD study of heat transfer in a fluidized bed. Chem Eng Sci 2017;172:310–22.